APPLICATION OF PRECONDITIONED, MULTIPLE-SPECIES, NAVIER-STOKES MODELS TO CAVITATING FLOWS

J.W. Lindau R.F. Kunz
Applied Research Lab, Penn State University, PO Box 30, State College, PA 16804-0030

S. Venkateswaran
University of Tennessee, Tullahoma, TN 37388

D.A. Boger
Applied Research Lab, Penn State University, PO Box 30, State College, PA 16804-0030

Abstract

A preconditioned, homogenous, multiphase, Reynolds Averaged Navier-Stokes model with mass transfer is presented. Liquid, vapor, and noncondensable gas phases are included. The model is preconditioned in order to obtain good convergence and accuracy regardless of phasic density ratio or flow velocity. Both incompressible and finite-acoustic-speed models are presented. Engineering relevant validative and demonstrative unsteady and transient two and three-dimensional results are given. Transients due to unsteady cavitating flow including shock waves are captured. In modeling axisymmetric cavitators at zero angle-of-attack with 3-D unsteady RANS, significant asymmetric flow features are obtained. In comparison with axisymmetric unsteady RANS, capture of these features leads to improved agreement with experimental data. Conditions when such modeling is not necessary are also demonstrated and identified.

1 Introduction

The ability to properly model multiphase flows has significant potential engineering benefit. In particular, sheet cavitation may occur in submerged high speed vehicles as well as pumps, propellers, nozzles, and numerous other venues. Traditionally, cavitation has had negative implications associated with damage and/or noise. However, for high speed submerged vehicles, the reduction in drag associated with a natural or ventilated supercavity has great potential benefit. Cavitation modeling remains a difficult task, and only recently have full three-dimensional, multi-phase, Reynolds-Averaged, Navier-Stokes (RANS) tools reached the level of utility that they might be applied for engineering purposes. Previously, Kunz et al. (2000) have developed and demonstrated a model capable of representing multiphase homogeneous mixture flows. Venkateswaran et al. (2001) adapted this development to finite-acoustic-speed multiphase compressible flow. In the current paper, the models of Kunz et al. (200) and Venkateswaran et al. (2001) are applied to engineering relevant flows. This will serve to further demonstrate and validate the capabilities of the multiphase RANS model.

Non-equilibrium mass transfer modeling is employed to capture liquid and vapor phasic exchange. The computational model, designated UNCLE-M, can handle buoyancy effects and the presence/interaction of condensable and non-condensable fields. This level of modeling complexity represents the state-of-the-art in CFD analysis of cavitation. The restrictions in range of applicability associated with inviscid flow, slender body theory and other simplifying assumptions are not present. In particular, the code can plausibly address the physics associated with high-speed maneuvers, body-cavity interactions and viscous effects such as flow separation.

The principal interest here is in modeling flow fields dominated by attached cavities. These are presumed to be sheet cavities amenable to a homogeneous approach. In other words, it is presumed that nonequilibrium interface dynamics are of negligible magnitude. In addition, for the configurations considered, interface curvatures are very small, thus the effect of surface tension is not incorporated.

In previous work (Kunz et al. 1999), the fidelity of UNCLE-M has been demonstrated for steady and unsteady fluid flows. In the work presented here, UNCLE-M will be applied to several configurations. Some of these configurations represent experimentally documented test cases. For others, the result demonstrates a capability to

capture a known, but rarely captured physical phenomenon. Model results will be presented for ventilated, vaporous, and combined ventilation and vaporous cavitation. Both steady (averaged) and unsteady behavior of the flow will be presented and compared with data. In addition, interesting unsteady numerical results will be presented in a field form for comparison with photographic data. Some of the most intriguing results are due to the fundamentally three-dimensional nature of turbulent multiphase flow. By comparison of the numerical, measured, and well understood, demonstrative results, reliability and capabilities of the numerical and physical modeling may be understood.

One of the complicating phenomena associated with underwater multiphase flows is the presence and effect of compressibility in a flow that is largely incompressible. For many applications, such as flow around a hydrofoil, this is due to the decrease, relative to any pure constituent phase, in acoustic speed for a multiphase mixture. Then velocities normally associated with subsonic, incompressible flows result in supersonic conditions and associated strong wave formations such as unsteady shocks (Arndt et al. 2000). To directly model flows containing shocks, a suitable representation of compressible flow is necessary. Also, in these flows, liquid vapor mass transfer is important. The goal here is to present, demonstrate and validate a three-dimensional, RANS based multiphase method capable of capturing the density ratios, Reynolds Numbers, Mach Numbers, and relevant flow features such as shocks and overall inherent and forced unsteadiness associated with these flows.

Nomenclature

C_ϕ	mass transfer model constants	t, t_∞, Δt	physical time, mean flow time scale, time step
C_d	drag coefficient	U	velocity magnitude
$C_Q \equiv \dot{Q}/(U_\infty d^2)$	ventilation flow coefficient	y^+	dimensionless wall distance $(\rho y U_t)/\mu_m$
c	sonic velocity	α	volume fraction
d	body diameter	ρ	density
f	cycling frequency (Hz)	σ	cavitation number ($\equiv \frac{p_\infty - p_c}{1/2\rho_l U_\infty^2}$)
$\dot{m}^-$, $\dot{m}^+$	mass transfer rates	**Subscripts, Superscripts:**	
p, p_c	pressure, cavity/vaporization pressure	d	body diameter
$\dot{Q}$	volumetric flow rate	l	liquid
Re_d	Reynolds number based on body diameter	ng	non-condensable gas
Str	Strouhal frequency $(fD)/U_\infty$	v	condensable vapor/vaporization
s	arc length along configuration	∞	free-stream/reference value

2 Model Equations

For the purposes of analysis and development of appropriate preconditioning, theoretical development of the underlying differential model has been presented previously (Kunz 2000 and Venkateswaran 2001). Here, the governing model equations solved for three-phase flow resemble the equations employed in single-phase multi-component reacting-gas-mixture flows. Both the incompressible and finite-acoustic-speed compressible constituent phase form of the equations are applied here. In the finite-acoustic-speed formulation of the three-phase equations, each constituent phase is governed by a linear state relation between density and pressure. This corresponds to a

constant acoustic speed for each isolated constituent phase but a mixture sound speed dependent on constituent make-up and local pressure. Similarly to the previous presentations, here, the equations for each formulation are solved in an absolutely conservative fashion. A standard high Reynolds number form of the $k-\epsilon$, two-equation model with wall functions provides turbulence closure. The eigenvalues of the associated systems and the preconditioning forms have been previously discussed and lead to good convergence and accuracy at all phasic density ratios and flow velocities. Therefore, the model equations are not presented here.

In the finite-acoustic-speed model, the density of each constituent is linearly dependent on pressure. This linearized compressibility is based on a constant constituent phasic speed of sound. This is sufficient to resolve the correct isothermal sound speed for the homogeneous mixture as a function of the constituent volume fractions. The correct mixture sound speed is clearly represented in the eigenvalues of the inviscid flux Jacobians. In fact, as is well known, analysis of the flux Jacobians is a proper method for deriving the acoustic speed, and the resulting expression is given in Equation 1. From this equation, the dramatic effect of sound speed attenuation due to mixture flows may be seen. This is presented in Figure 1 for a representative liquid vapor mixture.

$$c = \frac{1}{\sqrt{\rho\left(\frac{\alpha_l}{\rho_l c_l^2} + \frac{\alpha_v}{\rho_v c_v^2} + \frac{\alpha_{ng}}{\rho_{ng} c_{ng}^2}\right)}} \qquad \textbf{(1)}$$

Additional Physical Modeling

The finite rate mass transfer model equations solved here have been described previously (e.g. Kunz 2000). The mass transfer terms appear in the continuity relations pertaining to conservation of liquid and vapor. For transformation of liquid to vapor, $\dot{m}^-$ is modeled as being proportional to the product of the liquid volume fraction and the difference between the computational cell pressure and the vapor pressure. This model is similar to the one used by Merkle et al. (1998) for both evaporation and condensation. For transformation of vapor to liquid, a simplified form of the Ginzburg-Landau potential is used for the mass transfer rate $\dot{m}^+$. The terms themselves represent either a source or sink in the continuity relations. Recall that in the present approach, there are a number of continuity relations equal to the number of phases, and, in an absolutely conservative formulation, either mass or mixture volume may be conserved variables. Relations for liquid destruction and liquid production are given in Equation 2.

$$\dot{m}^- = \frac{C_\phi \rho_v \alpha_l MIN[0, p - p_v]}{\left(\frac{1}{2}\rho_l U_\infty^2\right) t_\infty} \qquad \dot{m}^+ = \frac{C_\phi \rho_v (\alpha_l - \alpha_{ng})^2 (1 - \alpha_l)}{(500) t_\infty} \qquad \textbf{(2)}$$

C_ϕ is an empirical constant. Both mass transfer rates are nondimensionalized with respect to a mean flow time scale. For all work presented here, $t_\infty = 1$ and $C_\phi = 10^5$. These values were arrived at by an investigation of average attached cavity lengths over ogives and comparison with experimental results of Rouse and McNown (1948). A demonstration of the comparison and sensitivity to the values of the constants are given in Figure 2.

3 Numerical Method

The described model equations are solved in the UNCLE-M code. This code has its origins as the UNCLE code, developed for incompressible flows at Mississippi State University (Taylor et al. 1995). Later this code was extended to multiphase mixtures, substantially revised, and named UNCLE-M (Kunz 2000). The code is structured, multi-block, implicit and parallel with upwind flux-difference splitting for the spatial discretization and Gauss-Seidel relaxation for the inversion of the implicit operator. Primitive variable (MUSCL) interpolation with van Albada limiting was applied to retain higher order accuracy in flow fields containing physical discontinuities. In keeping with the finding of Kunz (2000), only those source terms associated with vapor production were linearized for inclusion in the implicit linear system left-hand-side. Terms associated with liquid production were treated explicitly and under-relaxed with a factor of 0.1. At each pseudo-time step, the turbulence transport equations were solved subsequent to solution of the mean flow equations. During this investigation, attention was given to the necessity of temporal and spatial discretization independence. As a requirement, to accommodate the use of wall functions, for regions of attached liquid flow, fine-grid near-wall points were established at locations yielding $10<y^+<100$. Further details regarding the numerical method are available in Kunz (2000).

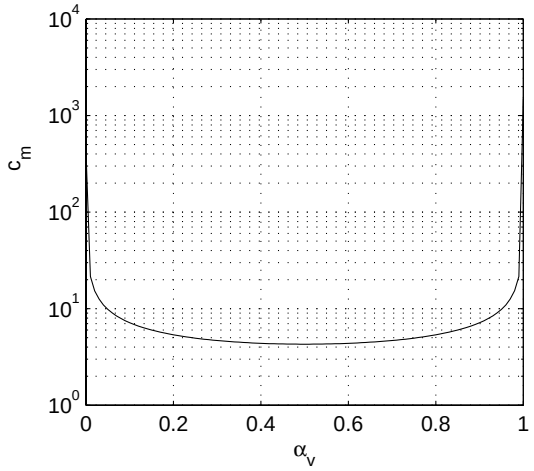

Figure 1: Homogeneous isothermal liquid-vapor mixture sound speed versus vapor volume fraction. Liquid sound speed, 1500m/s. Pure vapor sound speed 429m/s. Pure liquid density 1000kg/m^3. Pure vapor density 0.025kg/m^3. From Equation 1.

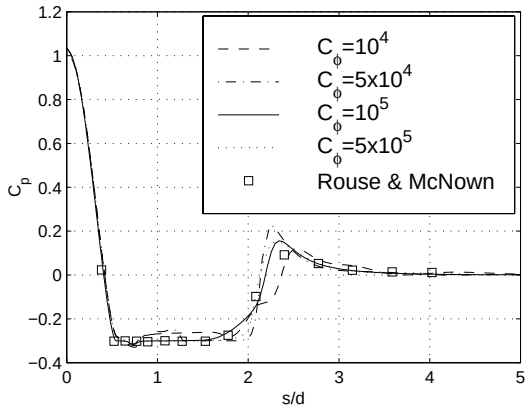

Figure 2: Comparison of effect of rate constants (Equation 2) and experimental data (Rouse and McNown 1948) for naturally cavitating flow over a hemispherical head and cylindrical afterbody. Steady, incompressible constituent phase (infinite sound speed) model results.

4 Results

Model results are presented capturing unsteady and transient flows. Two-dimensional, axisymmetric, and fully three-dimensional cases have been included. It is the intention here to resolve the physics necessary to render the flowfield during partial or super cavitation. Each of these cases represents a relatively complex time-dependent engineering flow and illustrates the utility of the method for a variety of two and three phase flows with and without mass transfer. In each case, the density ratio of the liquid phase to the gaseous phases is three or more orders of magnitude. Some of these cases are presented in comparison to experimentally obtained data. Therefore, these results serve to further validate for the modeling method. This validation has been previously initiated (Kunz 2000, Kunz 1999, and Lindau 2000).

Cavitating Flow in a Venturi

Stutz and Reboud (1997) and Reboud et al. (1998) have performed detailed unsteady, flowfield measurements of vaporous cavitating flow in the two-dimensional Venturi section of a water tunnel. The test section captures significant physics found on the suction side in a blade passage. Thus their experiment and the current model results represent partially cavitating flow in a turbomachinery-like environment. In Figure 3, the average and RMS fluctuating portions of the liquid volume fraction is presented based on the modeled flow. This figure serves to

illustrate the geometry of the modeled test section as well as the results obtained during modeling. The test section had a height at the throat equal to 43.7 mm and a constant width equal to 44 mm. The nominal cavity length for comparison here was 80 mm in the horizontal direction. The experiments were conducted at Reynolds numbers based on cavity length from $4.3x10^5$ to $2.1x10^6$ and at a range of cavitation numbers, based on the upstream pressure and velocity, from 0.6 to 0.75. It may be seen from the figure that although there is a high degree of unsteadiness in the region of the cavitating flow, this unsteadiness is confined to the test section area. This is consistent with the commentary of Reboud et al. (1998).

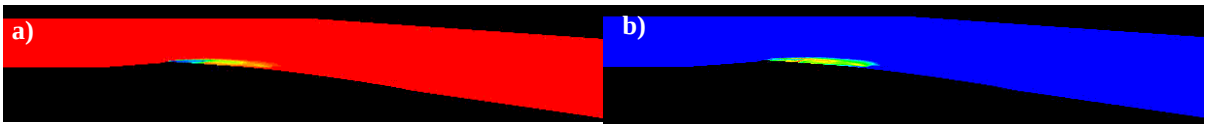

Figure 3: Computational result. Unsteady, naturally cavitating, two-dimensional flow. $Re_L=7.1x10^5$ (based on cavity length). Modeling of a two-dimensional cavitation tunnel. Reported in Stutz and Reboud (1997).
a) Mean liquid volume fraction. Red=1. Blue=0.
b) RMS fluctuating component of liquid volume fraction. Red=0.5. Blue=0.

In Figure 4, the current computational results are presented with the experimental data of Reboud et al. (1998). It is apparent that the unsteady model results are in reasonable agreement with the experiments. In the figure, results have been plotted at the five measurement stations used in the experiments. Each of these stations is given at a horizontal position. The experimental cavity was initiated due to the suction peak on the lower surface of the throat of the test section, a reference position of x=0. Based upon these results, the relative closeness of the model to experimental cavities was judged reasonable. In part (a) of the figure, the mean vapor volume fraction is plotted at the five axial stations. Considering the great difficulty in capturing flow detail in an unsteady two-phase flow, the level of agreement shown is again, reasonable. Clearly the model tends to over estimate the void fraction, particularly at the forward region of the cavity, at x=22.5mm. However, the average quantities are in excellent agreement at the tail end. Similarly reasonable agreement is demonstrated with the unsteady portion of the RMS void fraction, part (b). Here the error is greater in the closure region, at x=60mm and x=80mm. Considering the difficulty of modeling in the closure region, this level of agreement is also reasonable. In part (c), the average axial velocity is given at the five measurement stations. It should be noted that, by application of a two-phase Navier-Stokes model based on a barotropic state law, Reboud et al. (1998) were able to obtain similarly good agreement with the experimental data.

The finite-acoustic-speed form of UNCLE-M was also applied to this two-dimensional cavitation tunnel experiment. In Figure 5, a particularly interesting result is shown. At four points in time, the evolution of a model cavity collapse has been illustrated. At each time step shown, in the upper portion of the figure, the liquid volume fraction is shown. Here the capabilities of the finite-acoustic-speed model to tackle problems associated with cavitation damage have been demonstrated. During the initial transient, prior to establishment of a cavity cycle, both the incompressible and finite-acoustic-speed forms of UNCLE-M exhibited a high degree of unsteadiness and some cavity pinching. However, in the incompressible model, the collapse of the pinched cavity does not lead to a significant overpressure. As has been discussed, the finite-acoustic-speed model has the physical mechanism to translate a cavity collapse into a nonlinear pressure wave that rapidly coalesces into a shock. It has been demonstrated previously (Venkateswaran 2001) that the finite-acoustic-speed model contains the proper physics needed to correctly track unsteady two-phase shock waves. Here the physical mechanism to evolve the collapse of a cavity and subsequent shock wave formation and evolution has been shown.

Ventilated Axisymmetric Cavity Flow

Stinebring et al. (1979 and 1983) have performed steady and unsteady flow measurements of ventilated cavity flow over a conical head and cylinder. Here, the model results based on three different ventilation flow rates are compared to data. In their experiments, a 45^o cone and cylindrical afterbody were assembled with six ventilation ports. The ports were 0.635 mm in diameter and were installed, at equal circumferential intervals, just downstream of the corner joining the cone and cylinder. Flow of noncondensable gas through these ports was precisely controlled and relevant cavity data were recorded with several methods described by Stinebring et al. (1979 and 1983). Experimental results obtained at Reynolds numbers, based on model diameter, from 230,000 to 390,000 were compared to the computational model. For the model, the Reynolds number was 136,000 and the ports were modeled by inserting noncondensable gas, perpendicular to the free stream over a region of 0.635 mm in axial extent, just downstream of the corner joining the cone and cylinder. Due to the fully turbulent nature of the computational model and the domination of the flowfield by the separated two-phase region, it is suspected that the discrepancy in Reynolds numbers should have little effect on the overall results

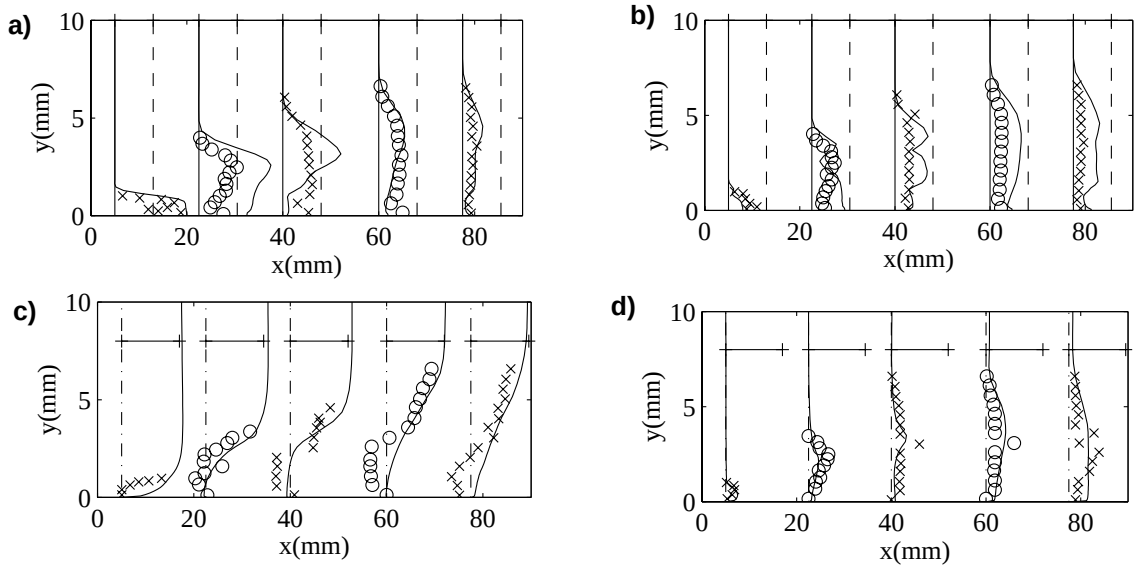

Figure 4: Comparison of modeled, unsteady cavitating flow to measurements at five horizontal stations (Reboud et al. 1998). y-vertical distance from wall. x-horizontal distance downstream of throat.

a) Mean vapor volume fraction (α_v).
b) Fluctuating RMS vapor volume fraction.
(Solid line indicates α_v=0. Dashed line indicates α_v=0.5.)

c) Mean horizontal velocity.
d) Fluctuating RMS horizontal velocity.
(Horizontal bars at stations indicate relative scale of a 12m/s velocity, the approximate free stream).

Figure 6 contains illustrative results from the modeled ventilated cavity flow over the cone and cylinder. The ventilation flow rate is given, nondimensionally, in terms of a flow coefficient, C_Q. Contours of modeled liquid volume fraction are shown with selected streamlines. Red indicates pure liquid, and blue indicates pure gas. As illustrated by the streamlines, the gas cavity is dominated by recirculating flow. This flow tends to periodically eject gas downstream. This ejection concurs with periodic modulation of the cavity shape. As may also be seen in the figure, the outer boundary of the cavity is also concurrent with a streamline. Hence the profile drag of the ogive is modulated at the same frequency. This modulation occurs at a frequency similar to the rate observed for vaporous cavities. The frequency of cavity modulation is at a rate determined by the mean length of the cavity. For flows over ogives at zero angle of attack and moderate cavitation numbers, this mean length is determined by the cavity pressure which is equivalently represented as the cavitation number (Stinebring and Holl 1979). Thus, the cycle frequency is roughly independent of whether the cavity is vaporous or ventilated. However, for a given cavitation number, the dominant periodic motion of ventilated cavities is less prominent than during vaporous cavity flow (Stinebring et al. 1983).

Figure 7 (a) contains a comparison the modeled and measured cavitation numbers for given ventilation flow coefficients. The cavity number, σ, is determined by the average minimum pressure in the cavity downstream of the injector. In the model and in the experiments, the cavity pressure, p_c, was found approximately one model radius downstream of the port. This serves to illustrate a difference between the modeled flow which is truly axisymmetric, and the actual flow which is most appropriately described as periodic. Fortunately, in the discussion of the experiments (Stinebring and Holl 1979) it was noted that the cavity length should be well correlated with the cavitation number. This relation is shown in Figure 7 (b). Here the model cavity pressure has been presented as a cavitation number and compared with measurements from Stinebring and Holl (1979). As is clear in the figure, the model results agree with the measurements, and comparison of other physical phenomena is made based on cavitation number rather than ventilation flow rate.

In Figure 8, a portion of the drag history, defined as the integrated axial pressure force normalized by the free stream dynamic head (May 1975), from modeled flow over a ventilated cone and cylinder at ventilation flow rate of C_Q=0.05 (σ=0.26) is shown. Here the rather complex model cycle is illustrated over an approximate period. The cycle is more easily discerned by comparison of the drag history to the evolving flowfield in Figure 9. Here, the same model cycle is presented with contours of liquid volume fraction around the region of the cavity flow.

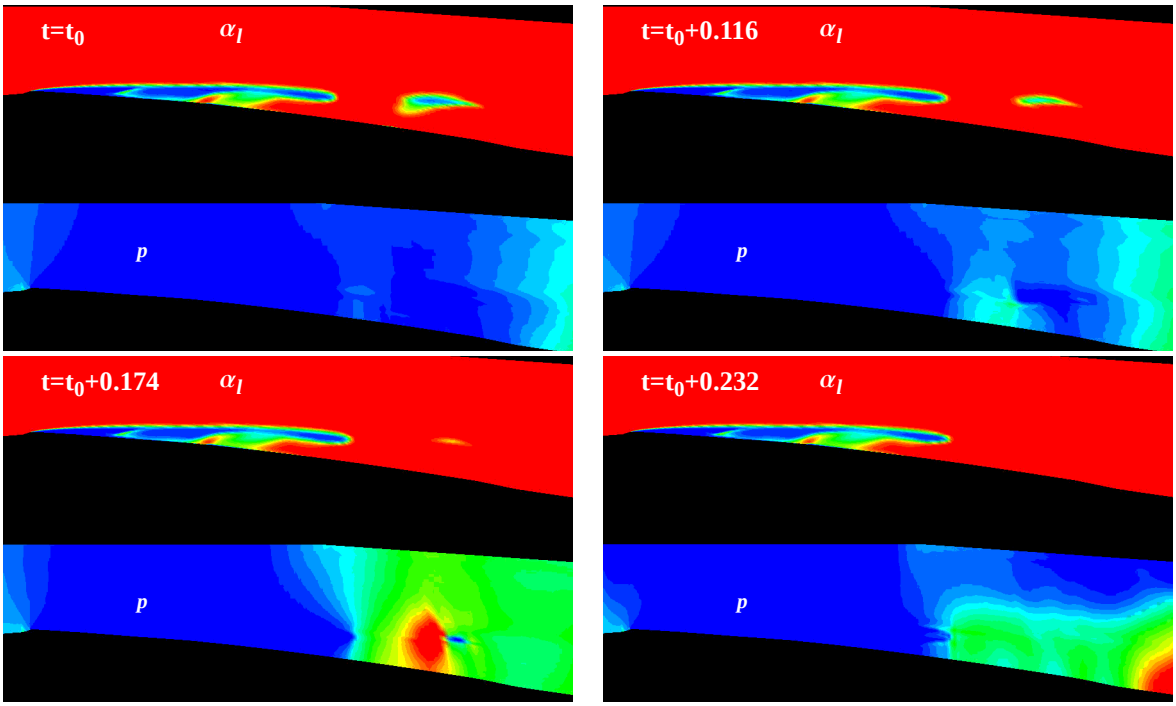

Figure 5: Finite Acoustic Speed Model. Flow during collapse of a pinched cavity. Liquid volume fraction: Red, α_l=1. Blue α_l=0. Pressure: Red, $p \geq 0.7\frac{\rho_l U_\infty^2}{2}$. Blue, $p \leq -0.7\frac{\rho_l U_\infty^2}{2}$.

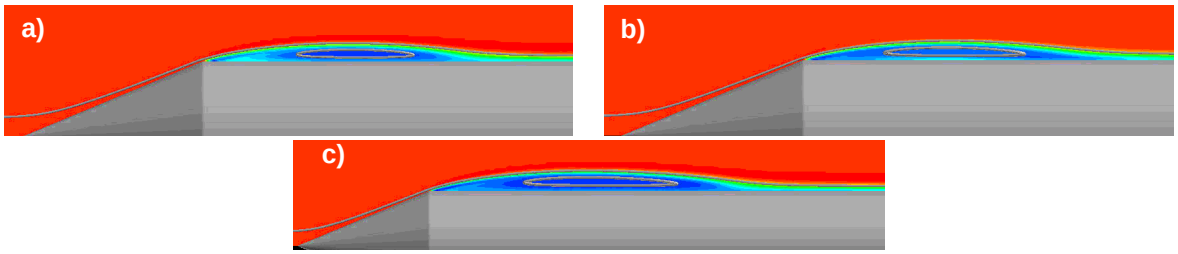

Figure 6: Snapshots of unsteady, modeled ventilated cavity flow over a conical head and cylinder. Contours of liquid volume fraction and selected streamlines. Red=1. Blue=0.
a) C_Q=0.039.
b) C_Q=0.05.
c) C_Q=0.078. (To better illustrate the cavity flow, (c) is presented in a reduced size relative to (a) and (b).)

In Figure 9, the oscillatory behavior of the cavity flow is well illustrated. The coloring has been adjusted such that a liquid volume fraction value greater than 0.5 is flooded red, and values of zero are dark blue. Thus the differences of volume fraction within the cavity is shown in greater detail, and the complete cavity cycle may be discerned. It is notable, as illustrated in Figure 8, that the cycle is made up of multiple local maxima in profile drag. This fits with the previously mentioned experimental observation regarding the lack of prominence of a dominant frequency during ventilated cavitation. Thus the cycle is complex and not readily obtained from zero-dimensional information such as drag history. The complete cycle, in the figures, is denoted by the first and last local drag minima shown. By carefully stepping through time history snapshots such as shown in Figure 9, and comparing these to the drag history, it was possible to determine the appropriate definition of the period.

In Figure 10, modeled and measured cavity cycling frequency is compared for ventilated flow over the conical head and cylinder. Here the experimental results (Stinebring et al. 1983) over a range of cavitation numbers and at three free-stream values of velocity are compared to the modeled flow. The modeled flow is given at three cavitation numbers, 0.2, 0.26, and 0.28. The agreement with data at the lowest cavitation number (highest dimensionless

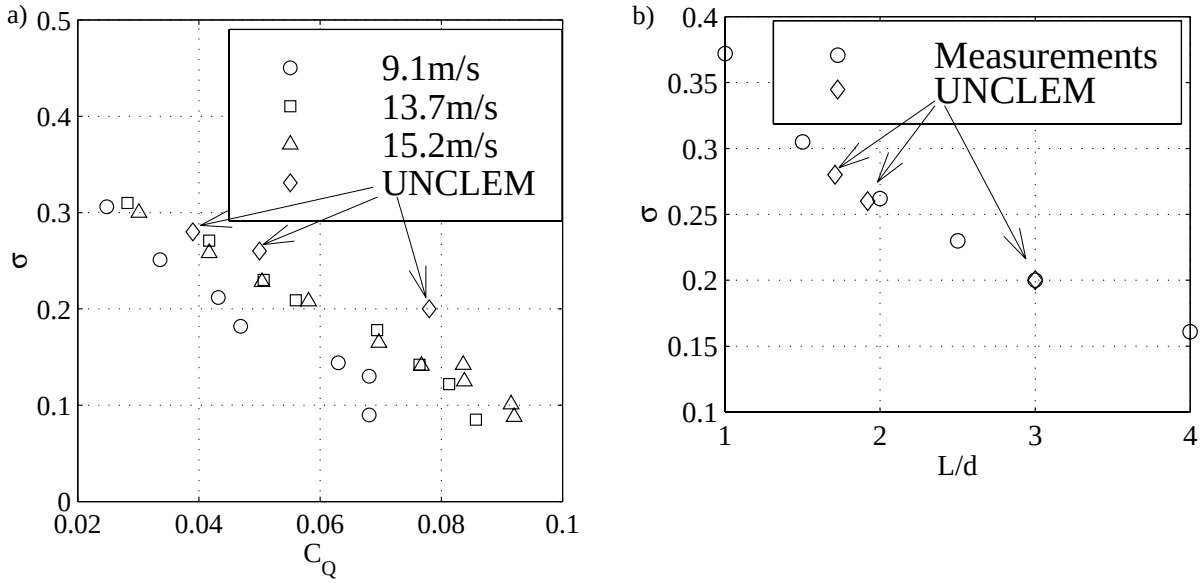

Figure 7: Comparison of modeled and measured (Stinebring and Holl 1979) ventilated cavity flow over a conical head and cylinder.
a) Cavity pressure, σ, versus ventilation rate, C_Q. b) Cavity pressure, σ, versus cavity length L/d.

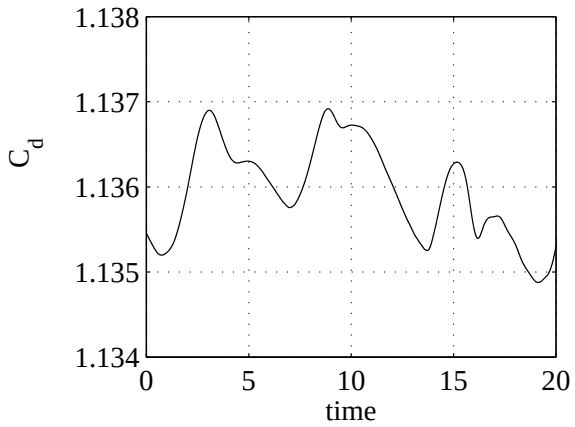

Figure 8: Profile drag, C_d, history spanning an approximate model cycle. Dimensionless time, tU_∞/d. Modeled ventilated cavity flow over a conical head and cylinder. C_Q=0.05.

ventilation rate) is excellent. At the higher cavitation numbers, there is a small divergence of modeled results from the measurements. However the proper trends are well captured. In addition, at lower ventilation flow rates, the spacing of the ventilation ports and other important length scales become larger relative to the cavity length. Thus, it is suspected that unmodeled three-dimensional effects on cavity behavior will be more significant at lower ventilation flow rates.

Fully Three-Dimensional Naturally Cavitating Flow

Turbulent, naturally cavitating flow over axisymmetric bodies is known to be a highly nonlinear and three-dimensional event. This is clearly illustrated in Figure 11. Here, a photograph during water tunnel testing of a blunt cavitator at zero angle-of-attack, $\sigma \cong 0.35$, and $Re_d \cong 150{,}000$ is shown in part (a) to be compared and contrasted to the model result in part (b). To obtain the model result, turbulent vaporous cavitating flow over a blunt cavitator was modeled. σ was set to 0.4 and Re_d was 148,000. An appropriate high Reynolds number grid with approximately 1.2 million nodes was used. The snapshot of part (b) represents a physical time slice taken after a clear model cavity

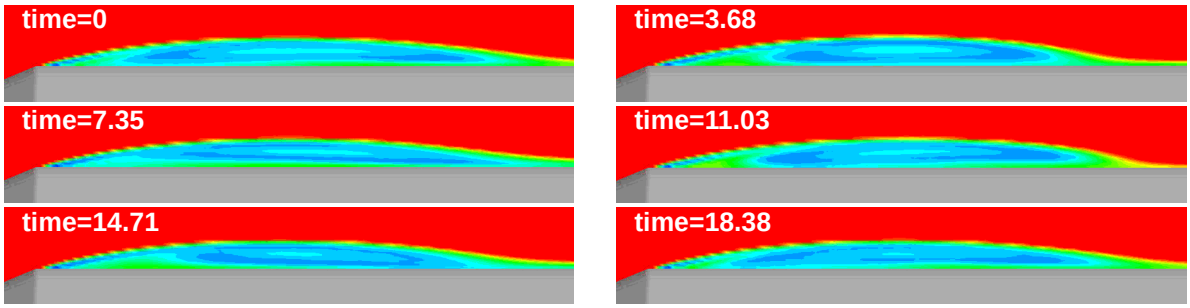

Figure 9: Modeled ventilated cavity cycle. C_Q=0.05. Liquid volume fraction contours. Red>0.5. Blue=0. Time given in dimensionless units, tU_∞/d.

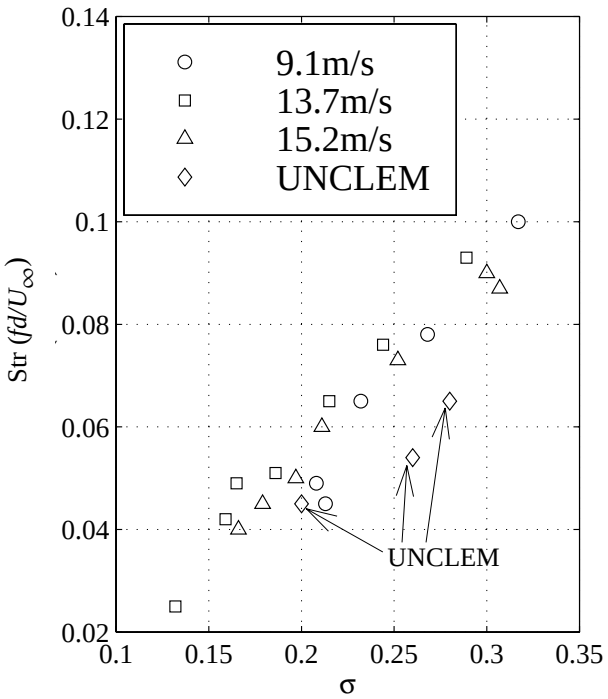

Figure 10: Comparison of modeled and measured (Stinebring et al. 1983) ventilated cavity flow over a conical head and cylinder. Cavity cycling frequency versus cavity pressure.

cycle had been established. In the figure, an isosurface at α_l=0.5 has been presented with selected streamlines, and the surface of the cylinder has been colored by volume fraction. The streamlines are merely suggestive (but helpful), as they have been generated based on instantaneous velocity vectors. Clearly in neither the model result nor the photograph is the flowfield in and around the cavity axisymmetric. It is suspected that physical, chaotic, dynamic interdependencies are responsible. For instance, there is little likelihood of obtaining purely axisymmetric conditions in even the most well controlled environments. Even the identification of all factors necessary to be controlled is a difficult task. This is compounded by the influence of highly nonlinear turbulent flow dominated by phase transition, etc. It is not suggested that, in obtaining the result of Figure 11 (b), the exact causal mechanism of the three dimensional and unsteady flow has been reproduced. Rather it is suggested that via an adequate level of modeling, the real flow has been well captured. Positive understanding of the causal mechanisms is a subject for further research.

Here a striking example of the divergence of three-dimensional and axisymmetric modeling is given. A sample of the results obtained by three-dimensional modeling of vaporous cavitation over a blunt ogive at zero angle of attack are presented in Figure 11 (b) and Figure 13. These results appear to agree with both significant qualitative and quantitative experimental observations. As in the experiment, the modeled reentrant flow has been observed to

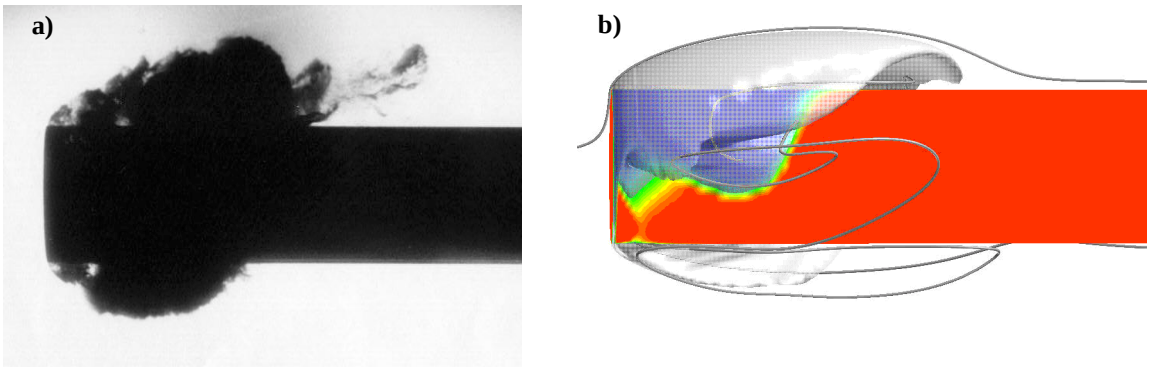

Figure 11: Blunt cavitator at zero angle-of-attack:
a) In water tunnel at $\sigma \cong 0.35$. (Stinebring 1976)
b) Model result from UNCLE-M at $\sigma = 0.4$. Isosurface (translucent) at $\alpha_l = 0.5$. Selected (instantaneous) streamlines. Surface of cylinder colored by α_l. Red=liquid. Blue=vapor.

follow a helical pattern. This helical flow revolves around the circumference of the cylinder. This revolution is driven by a complex reentrant flow. The flow emanates from the high pressure region downstream of the cavity. This high pressure region is situated at the aft end of the azimuthal section of the cavity of greatest axial extent. This area of the surface of the cylinder contains the stagnation point of an imaginary *streampath.* This streampath follows the outer edge of the cavity along that azimuthal sector. It is recalled again that the cavitation number of flow over axisymmetric bodies is highly correlated with mean cavity length. Thus, at that instant in time, this streampath traces a cavity profile representing an instantaneous minimum cavitation number. A maximum instantaneous cavitation number is similarly related to the axial streampath outlining the cavity of minimum axial extent. The correct cavitation number lies between this minimum and maximum. The reentrant flow tends to move away from this stagnation region. During its initial formation, due perhaps to turbulent fluctuations, the reentrant flow was initially driven and then moved permanently in a helical path. At the same time the helical path was established, other aspects of the flow tended to cause a cavity cycle that is largely axial. This axial cycle fits the typical observations of reentrant flow (Stinebring et al. 1979, 1983, and May 1975). This axial motion is observable in the snapshots and is also well captured by the profile drag coefficient history given in Figure 12. Here the drag history has been given over a model cycle as defined by the three-dimensional flow. Clearly the zero-dimensional drag coefficient is insufficient, by itself, to provide the true model cycle. However by examination of Figure 12 in conjunction with Figure 13, snapshots of the three-dimensional flowfield, it is possible to deduce the model cycle. The axial cycle may be nearly modeled, in a linearized simplification, as superimposed on the previously discussed circumferential motion. The circumferential motion is not divisible precisely by an integer number of axial periods. In fact the axial cycle is not regular and has a poorly defined amplitude. Therefore, this cavity cycle is appropriately described as nonlinear and quasi-periodic.

Due to the observed helical (not symmetric) nature of the reentrant region, it was necessary, experimentally, to use high speed movies to determine the period cavity cycling (Stinebring 1975, 1983, and personal communications). Generally two consecutive observed cycles were required to determine the reported cycle. This would then coincide with the cycle determined by a complete revolution of the reentrant jet. This is the cycle reported in three-dimensional model results of Figure 14. Here the model results from the current three-dimensional modeling are compared with previous two-dimensional results (Lindau 2000) and experimental observations (Stinebring 1983).

Three-Dimensional Supercavitating Transient

The authors are also interested in the hydrodynamic performance of supercavitating vehicles in maneuvers. Of particular interest are predicted transient forces and moments, as well as transient cavity behavior, which are important in the design of vehicle control systems and gas ventilation schemes.

In Figure 15 we present a set of preliminary prescribed motion results for a notional supercavitating vehicle. Figure 15 (a) illustrates a view of the geometry, which has a relatively blunt cavitator and three annular ventilation ports with aft oriented gas deflectors. A cavity gas ventilation rate is prescribed that is sufficient to enshroud the entire vehicle during steady flight. A gas propellant flow rate is also specified at the exhaust nozzle. For this analysis, the gas flow is assumed incompressible. A prescribed pitch-up-pitch-down maneuver is specified (see Figure 15 (i). A non-dimensional timestep of $\Delta t/t_{ref} = .09473$ was specified, where $t_{ref} = L_{vehicle}/U_{\infty}$. A 1,218,536 vertex grid was used. The simulation was run on 48 processors of a Cray T3E. Figure 15 (b) through (h) shows several snapshots of the evolving cavity during the maneuver, as designated by isosurfaces of liquid volume fraction

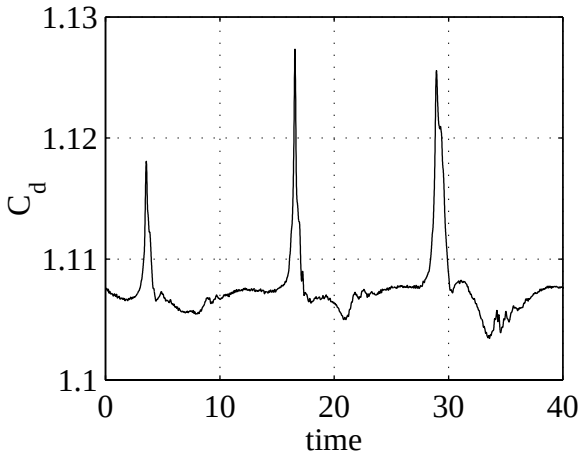

Figure 12: Profile drag, C_d, history spanning an approximate model cycle. Dimensionless time, tU_∞/d. Modeled vaporous cavity flow over a blunt cylinder, σ=0.275.

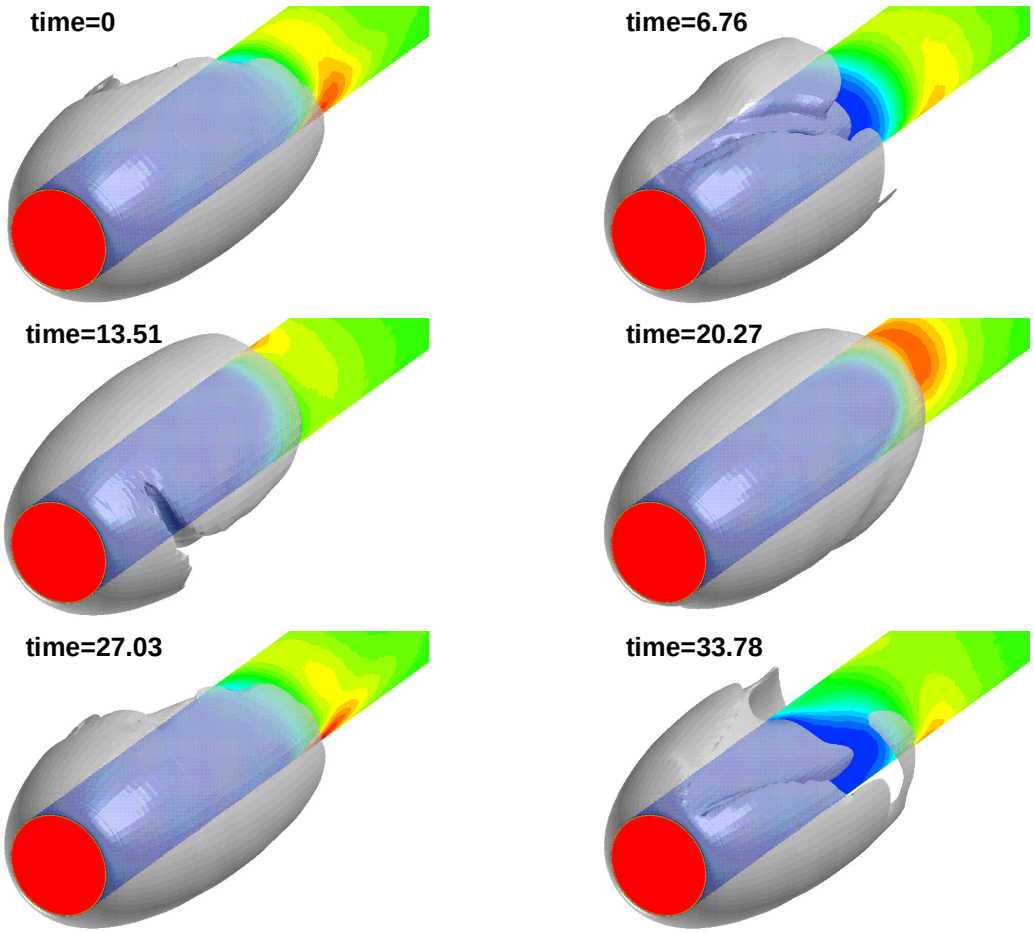

Figure 13: Snapshots of modeled vaporous cavitation. σ=0.275. Translucent isosurface at α_l=0.5. Surface of cylinder colored by pressure.

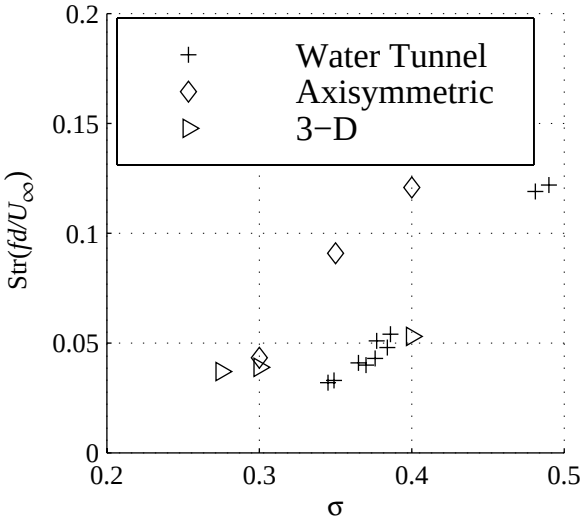

Figure 14: Cavity cycling frequency versus cavitation number. Vaporous cavitation over blunt cylinder. Comparison of experimental (Stinebring et al. 1983), model axisymmetric, and model three-dimensional results.

= 0.5. A three-field simulation was carried out. Vaporous cavitation occurs upstream of the first gas deflector. Clearly evident is the significant perturbation in the cavity for this maneuver. Indeed, the cavity intersects the body at t/t_{ref} = 47.4. Also, natural cavitation near the leading edge is not sufficient to keep the first injection port unwetted. Figure 15 (i) shows the predicted lift history for the vehicle during the maneuver, as well as the prescribed angle-of-attack.

5 Summary and Conclusions

A model formulation for the computation of multi-phase mixture flows with appropriate preconditioning resulting in an inviscid system, with well conditioned eigenvalues, independent of density ratio, has been applied. In this model, designated UNCLE-M, flows are assumed to be in homogeneous equilibrium, and each phase is represented as a separate species with an attendant equation of state. In the computational implementation, the model allows finite rate mass transfer to take place between a liquid and vapor phase, and maintains an additional phase for the representation of a noncondensable gas.

Results have been given demonstrating capabilities of the computational model. Complex two-dimensional, three-dimensional, and unsteady representative and validative flows have been examined. Supportive experimental results have been included, and detailed discussion of the modeled flow features has been given. The differential and computational form as well as the solution of the fully three-dimensional, three-phase model with mass transfer has been presented.

The validative results include modeled vaporous cavity flow in a Venturi section previously reported by Stutz and Reboud (1997) and Reboud et al. (1998), modeled ventilated cavity flow over a conical forebody and cylinder previously reported by Stinebring et al. (1979 and 1983), and modeled vaporous cavitating flow over a blunt cylinder previously reported by Stinebring et al. (1983). In each of these cases the flow was unsteady, complex, and almost certainly three-dimensional. In the case of the Venturi (Reboud et al. 1998), two-dimensional model results were good considering the complex unsteady nature of the flow and the high level of detail provided by the experimental results. However, the transverse (not modeled) dimension of the test section was 44 mm while the height was 43.7 mm. Based on other modeling and experimental evidence offered here, it is suspected that three-dimensional modeling of such a Venturi section would be useful.

In the case of the flow over axisymmetric bodies at zero angle of attack, it is significant that the axisymmetric modeling of ventilated cavitation is apparently sufficient while the model results for vaporous cavitation shown in Figure 14 and reported (Lindau 2000) are not. A suspect cause for this difference is fairly straightforward. In the tested, ventilated, conical cavitator, ventilation ports were installed at six circumferentially distributed locations, equidistant apart, just aft of the corner joining the cone to the cylinder. Thus the ventilation ports would tend to continuously feed the cavity in a symmetric manner. It is likely, even in the presence of strong flow nonlinearities, that this arrangement would have tended to reinforce symmetry. In addition compared to the blunt cylindrical cavitator, the lower drag conical head would be likely to produce a less violent, more symmetric flow in the cavity closure region. As is clear from the experimental evidence given in Figure 11, vaporous cavitation over blunt objects

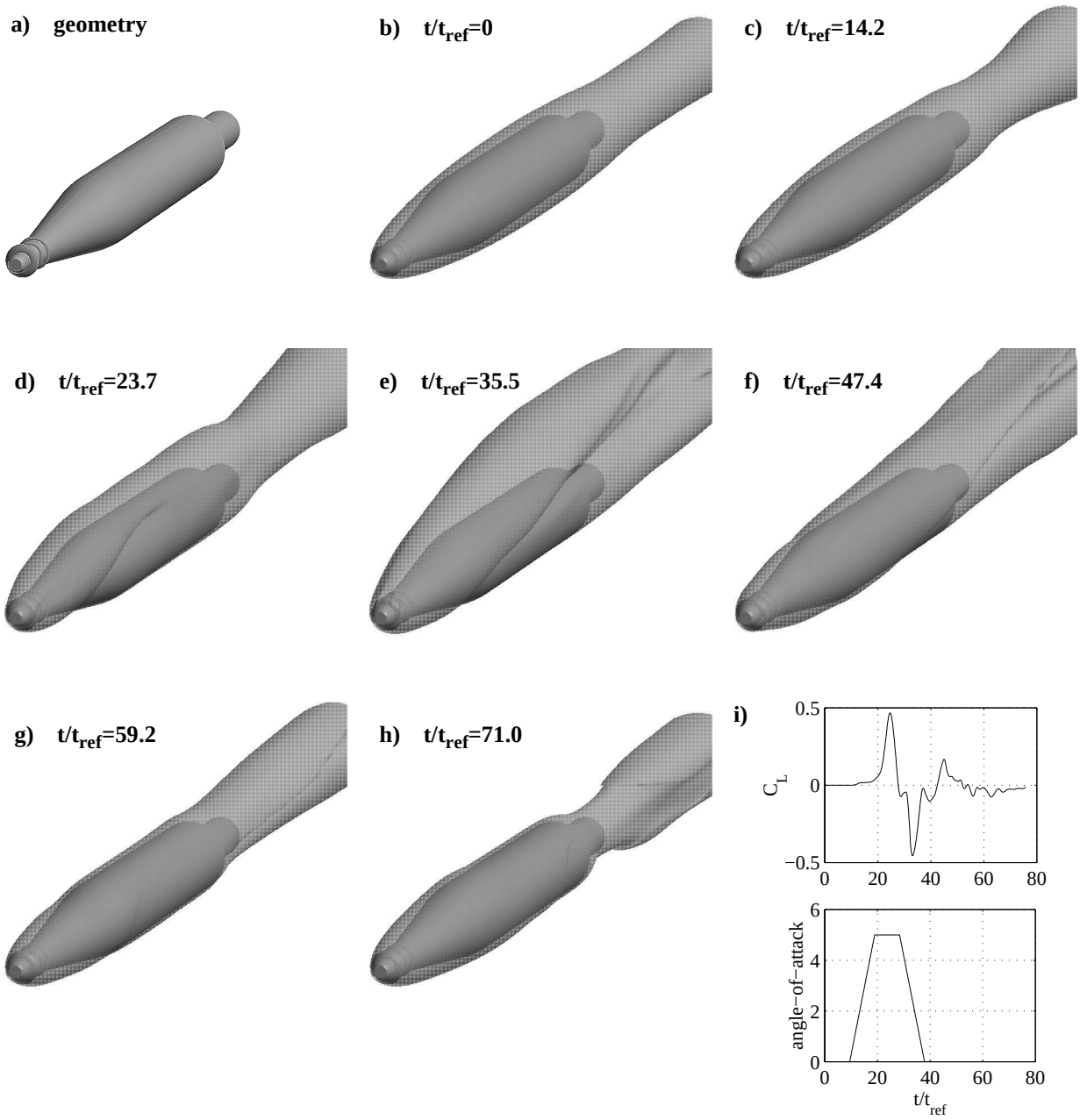

Figure 15: Elements of 3-D unsteady simulation of prescribed maneuver of a notional high speed supercavitating vehicle.
a) View of geometry.
b)-h) Cavity surface shape vs. time as indicated by isosurface of α_l= 0.5.
i) Prescribed angle-of-attack and lift history vs. time.

at moderate cavity numbers tends to be asymmetric. This would have been particularly true for higher drag objects at higher cavitation numbers. This is demonstrated in Figure 14, where the axisymmetric model cycle frequency tends to diverge from the experimental data as cavitation number is increased.

Success with geometrically simple validative results suggest that the modeling method may be applied to more complicated design level tasks with confidence. This has been demonstrated here in the case of a three-phase model of a supercavitating vehicle undergoing a transient maneuver. With future application of the newly formulated fully compressible model (Lindau 2001) planned for complex geometries, it is suspected that UNCLE-M will be a useful tool for supercavitating design efforts.

Acknowledgments

This work was supported by the Office of Naval Research, contract #N00014-01-1-0325, with Dr. Kam Ng as contract monitor. This work was supported in part by a grant of DoD 2001 Challenge Project HPC resources from the Army Research Laboratory Major Shared Resource Center and the Army High Performance Computing Research Center. The provision of information by Drs. Benoit Stutz and Jean-Luc Reboud is also appreciated. Also gratefully acknowledged is valuable input from Dave Stinebring.

References

Arndt, R.E.A., Song, C.C.S., Kjeldsen, M., He. J., and A. Keller (2000) *Instability of Partial Cavitation: A Numerical/Experimental Approach*, ONR 23rd Symposium on Naval Hydrodynamics, September.

Kunz, R.F., Boger, D.A., Chyczewski, T.S., Stinebring, D.R., and H.J. Gibeling (1999) *Multi-Phase CFD Analysis of Natural and Ventilated Cavitation about Submerged Bodies*, ASME Paper FEDSM99-7364.

Kunz, R.F., Boger, D.A., Stinebring, D.R., Chyczewski, T.S., Lindau, J.W., Gibeling, H.J., Venkateswaran, S., and T.R. Govindan (2000) *A Preconditioned Navier-Stokes Method for Two-Phase Flows with Application to Cavitation Predication*, Computers and Fluids, vol. 29, pp. 849-875, November.

Lindau, J. W., Kunz, R. F., Boger, D. A., Stinebring, D. R. and H.J. Gibeling (2000) *Validation of High Reynolds Number, Unsteady Multi-Phase CFD Modeling for Naval Applications*, Proceedings of ONR 23rd Symposium on Naval Hydrodynamics, Val de Reuil, France, Sept 17-22.

Lindau, J.W., Venkateswaran, S., Kunz, R.F. and C.L. Merkle (2001) *Development of a Fully-Compressible Multi-Phase Reynolds-Averaged Navier-Stokes Model*, 15th AIAA Computational Fluid Dynamics Conference, Anaheim, California, 11-14 June.

May, A. (1975) *Water Entry and the Cavity-Running Behaviour of Missiles*, Naval Sea Systems Command Hydroballistics Advisory Committee Technical Report 75-2.

Merkle, C.L., Feng, J., and P.E.O. Buelow (1998) *Computational Modeling of the Dynamics of Sheet Cavitation*, 3rd International Symposium on Cavitation, Grenoble, France.

Reboud, J., Stutz, B. and O. Coutier (1998) *Two-Phase Flow Structure of Cavitation: Experiment and Modelling of Unsteady Effects*, Third International Symposium on Cavitation, Grenoble, France, April.

Rouse, H. and J. S McNown (1948) *Cavitation and Pressure Distribution, Head Forms at Zero Angle of Yaw*, Studies in Engineering Bulletin 32, State University of Iowa.

Stinebring, D.R. and J.W. Holl (1979) *Water Tunnel Simulation Study of the Later Stages of Water Entry of Conical Head Bodies: Phase II - Effect of the Afterbody on Steady State Ventilated Cavities*, TM 79-206, The Pennsylvania State University, Applied Research Laboratory.

Stinebring, D.R., Billet, M.L., and J.W. Holl (1983) *An Investigation of Cavity Cycling for Ventilated and Natural Cavities*, TM 83-13, The Pennsylvania State University Applied Research Laboratory.

Stinebring, D.R. (1976) Scaling of Cavitation Damage, M.S. Thesis, The Pennsylvania State University, University Park, Pennsylvania, August.

Stutz, B. and J. Reboud (1997), *Two-Phase Flow Structure of Sheet Cavitation*, Physics of Fluids, Vol. 9., No. 12, December.

Taylor, L. K., Arabshahi, A., and D. L. Whitfield (1995) *Unsteady Three-Dimensional Incompressible Navier-Stokes Computations for a Prolate Spheroid Undergoing Time-Dependent Maneuvers*, AIAA Paper 95-0313.

Venkateswaran, S., Lindau, J.W., Kunz, R.F. and C.L. Merkle (2001) *Evaluation of Preconditioning Algorithms for the Computation of Multi-Phase Mixture Flows*, AIAA 2001-0279.